Radiochim. Acta **100**, 759–770 (2012) / **DOI** 10.1524/ract.2012.1948

Spectroscopic investigations of Np(V/VI) redox speciation in hyperalkaline TMA-(OH, Cl) solutions

By X. Gaona[1,*], J. Tits[2], K. Dardenne[1], X. Liu[1,#], J. Rothe[1], M. A. Denecke[1], E. Wieland[2] and M. Altmaier[1]

[1] Institut für Nukleare Entsorgung, Karlsruhe Institute of Technology, (KIT), P.O. Box 3640, 76021 Karlsruhe, Germany
[2] Laboratory for Waste Management, Paul Scherrer Institut, 5232 Villigen PSI, Switzerland

(Received October 6, 2011; accepted in revised form January 5, 2012)
(Published online July 30, 2012)

Neptunium(V/VI) / TMA-OH / XANES reference spectra / EXAFS

Summary. The redox chemistry of Np(V/VI) was investigated in ∼ 0.6 M tetramethylammonium hydroxide/chloride (TMA-(OH, Cl)) solutions with $9 \leq -\log[H^+] \leq 13.5$. Redox conditions were defined by the absence or presence of ClO^- as oxidizing agent (Na-salt, 5×10^{-3} M and 5×10^{-2} M). The high total Np concentration ($[Np]_{tot} \sim 2 \times 10^{-3}$ M) led to the precipitation of solid phases in some of the samples. The carbonate concentration (as impurity of TMA-OH) was $2–3 \times 10^{-3}$ M.

UV-vis/NIR spectra obtained from the supernatant in TMA-(OH, Cl) solutions and absence of ClO^- showed clear Np(V) features, identified as NpO_2^+, $NpO_2CO_3^-$ and $(NpO_2)_x(CO_3)_y(OH)_z^{x-2y-z}$. No NIR features were observed within 800 nm $\leq \lambda \leq$ 1300 nm for samples with ClO^-. XANES edge energies and features of these samples confirmed the predominance of Np(V) in the absence of ClO^- and Np(VI) in the presence of ClO^-, by comparison to XANES reference spectra of Np(III/IV/V/VI) prepared within the present work by *in-situ* electrolysis. A similar Np redox distribution was observed for the solid phases based on XANES and EXAFS measurements. EXAFS spectra indicative of $Np^VO_2OH(s)$ and $Np^{VI}O_3 \cdot xH_2O(s)$ were obtained for samples in absence and presence of ClO^-, respectively. The formation of a Na-Np(VI) phase in 5×10^{-2} M ClO^- and $-\log[H^+] \sim 12$ was also indicated from the EXAFS, chemical analysis and SEM-EDS.

These results indicate that Np(VI) aqueous species and solid compounds prevail far below the oxidation border of water in alkaline solutions and also far below the E_H border calculated with the current NEA data selection [1]. These observations are further supported by correlations of literature thermodynamic data for actinides (U, Np, Pu and Am), which predict the formation of $NpO_2(OH)_3^-$ and $NpO_2(OH)_4^{2-}$ aqueous species with stability constants ($\log^* \beta^\circ_{1,3}$ and $\log^* \beta^\circ_{1,4}$) similar to those available for U(VI).

1. Introduction

The chemical behaviour of neptunium is of special concern for the safe disposal of radioactive waste because of its long half life ($T_{1/2} = 2.14 \times 10^6$ a), its radiotoxicity and its redox sensitivity. In the early stages after the closure of the repository when reducing conditions have not yet been established, Np(V) is expected to dominate according to the current NEA thermodynamic data selection [1, 2].

The chemistry of Np(VI) under alkaline conditions is not well-known. In the aqueous phase, the formation of anionic species (*e.g.*, $NpO_2(OH)_3^-$ and $NpO_2(OH)_4^{2-}$) has been proposed, although no thermodynamic data are currently selected in the NEA reviews [1, 2]. In analogy to U(VI), the formation of solid Na- and Ca-neptunates can also be expected. The chemical behaviour of these aqueous species and solid compounds can be relevant in cementitious systems and $NaCl/CaCl_2$-dominated saline environments.

Tetramethylammonium hydroxide (TMA-OH) and tetramethylammonium chloride (TMA-Cl) have been used in this work as background electrolytes. As a bulky cation, TMA^+ has previously been considered for the study of the actinide aqueous speciation (*e.g.*, U(VI) [3, 4] and Np(V) [5]) because it minimizes the precipitation of solid phases (as occurring with Na^+, K^+ or Ca^{2+}). However, TMA^+ strongly influences the aqueous properties of the system (activity of water, density, *etc.* – see Tables A1 and A2 in Sect. A) [6] and, consequently, special attention must be taken for thermodynamic modelling or thermodynamic calculations in systems where it is used as background electrolyte (TMA-(Cl, OH)).

This study focuses on the aqueous and solid phase speciation of Np(VI) in alkaline TMA-(OH, Cl) solutions in order to constrain its stability field and redox border with Np(V). The work is also meant to provide a better description of systematic trends for the An(VI) series, where only U(VI) has been characterized in detail and extensive thermodynamic data has been made available, as well as to set the basis for experiments under repository relevant conditions (*e.g.*, in NaCl and $CaCl_2$).

2. Thermodynamic background

Only few studies are available on the aqueous speciation of Np(VI) in hyperalkaline conditions. Ermakov *et al.* [7] measured the potentials of the Np(V/VI) and Pu(V/VI) couples in aqueous LiOH solutions (2.5 M to 4.0 M). The

*Author for correspondence (E-mail: xavier.gaona@kit.edu).
Current address: Laboratory for Energy and Materials Cycles, Paul Scherrer Institut, 5232 Villigen PSI (Switzerland)

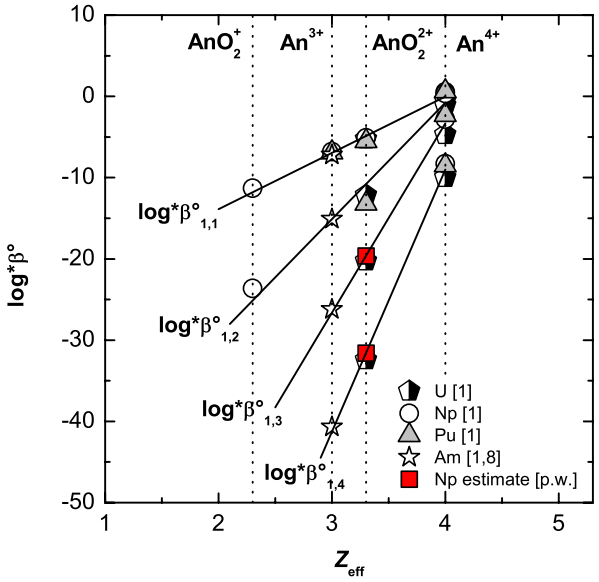

Fig. 1. Linear correlation of An(III/IV/V/VI) hydrolysis [$\log^* \beta^\circ_{1,n}$ ($n = 1$–4)] with Z_{eff} for An = Np, U, Pu and Am. All thermodynamic data as reported in [1], except for $Am(OH)_4^-$ [12]. Squares used for Np(VI) data estimated in this work.

review of these data in [2] provided upper limits for the hydrolysis constants $\log^* \beta^\circ_{1,3}$ and $\log^* \beta^\circ_{1,4}$ ($NpO_2(OH)_3^-$ and $NpO_2(OH)_4^{2-}$) (Table 1). If anionic oligomers exist (as they have been found in the uranium system), both values may be regarded as limiting [2].

Williams *et al.* [8] conducted extended X-ray absorption fine structure (EXAFS) measurements on the system Np(VI/VII) in 1 M NaOH. Starting from a Np(V) suspension, the authors promoted the oxidation to Np(VII) with a combination of ozone and electrolysis (+600 mV *vs.* Ag/AgCl). After collecting the EXAFS of Np(VII), the authors systematically reduced the potential applied until obtaining a pure Np(VI) EXAFS spectrum. Although no thermodynamic data can be extracted from this study, the structural parameters provided for the aqueous species forming in 1 M NaOH agree with those expected for $NpO_2(OH)_4^{2-}$.

The hydrolysis of actinides is known to correlate with their effective charge (Z_{eff}) [9]. Z_{eff} is directly the charge of the cation in trivalent and tetravalent actinides (+3 and +4, respectively). In the case of actinyl cations (AnO_2^+ and AnO_2^{2+}), the covalent bonding between the actinide and the two oxygen atoms enhances the charge of An in the equatorial plane, effectively resulting in 2.3 and 3.3, respectively [10]. Accordingly, and because of the similarities in their ionic radii, actinides with the same redox state tend to have similar hydrolysis constants. The linear correlation $\log^* \beta^\circ_{1,n}$ ($n = 1$–4) *vs.* Z_{eff} provided in Fig. 1 for Np, U, Pu and Am was used in order to estimate $\log^* \beta^\circ_{1,3}$ and $\log^* \beta^\circ_{1,4}$ for Np(VI) (see Table 1). Table 1 also provides $\log^* \beta^\circ_{1,3}$ and $\log^* \beta^\circ_{1,4}$ values reviewed and selected in [1, 11] for U(VI); these are accurate and well-defined stability constants, mostly selected from solubility experiments.

The relevance of the species $NpO_2(OH)_3^-$ and $NpO_2(OH)_4^{2-}$ is assessed in Fig. 2, where the predominance diagram of Np for $-0.8\ V \le E_H \le +1\ V$ and $10 \le pH \le 14$ has been calculated (a) in accordance with the current data selection of NEA, and (b) including the third and fourth hydrolysis species of Np(VI) estimated in the present work from its correlation with Z_{eff} ($\log^* \beta^\circ_{Correl}$). A significantly different picture is obtained when disregarding or including $NpO_2(OH)_3^-$ and $NpO_2(OH)_4^{2-}$. The latter case suggests a considerably smaller stability field of Np(V) in favour of a significantly larger Np(VI) stability field under hyperalkaline conditions.

Carbonate species of Np(V) and Np(VI) are expected to form under the conditions of this study. In addition to the Np(V/VI)-CO_3-OH species currently selected in the NEA thermodynamic data reviews, Neck *et al.* [13] reported the formation of the Np(V) species $NpO_2CO_3OH^{2-}$ and $NpO_2CO_3(OH)_2^{3-}$ (only conditional $\log \beta$ for $I = 3$ M $NaClO_4$ provided). Although not selected in the NEA review, the use of this $\log \beta_{1,1,2}$ was recommend in [2] for scoping calculations. Neither selection nor recommendation was issued in [2] for $\log \beta_{1,1,1}$, most likely because the formation constant in [13] was an estimate and "there was no direct experimental evidence for the formation of $NpO_2CO_3OH^{2-}$". The stability constants reported in [13] have been recalculated in this work to $I = 0$ by SIT (Table 2), using the $\varepsilon(Na^+, ML^{n-})$ estimates reported in [14]. These species have also been considered for thermodynamic calculations in Sect. 4.

Table 1. Reaction and $\log^* \beta^\circ$ values for the formation of $NpO_2(OH)_3^-$ and $NpO_2(OH)_4^{2-}$, as upper limits proposed in [2] (UL-NEA), calculated in the present work by correlation with Z_{eff} (Correl.), and selected in [1] for U(VI).

Reaction	$\log^* \beta^\circ_{UL\text{-}NEA}$ [2]	$\log^* \beta^\circ_{Correl.}$ [this work]	$\log^* \beta^\circ_{U(VI)}$ [1]
$NpO_2^{2+} + 3H_2O \Leftrightarrow NpO_2(OH)_3^- + 3H^+$	≤ -19	-19.6 ± 1.0	-20.25 ± 0.42
$NpO_2^{2+} + 4H_2O \Leftrightarrow NpO_2(OH)_4^{2-} + 4H^+$	≤ -33	-31.6 ± 1.0	-32.40 ± 0.68

Table 2. $\log \beta$ values for the formation of $NpO_2CO_3OH^{2-}$ and $NpO_2CO_3(OH)_2^{3-}$ as reported in [13], and recalculated to $I = 0$ in this work.

Reaction	$\log \beta_{1,n,m}$ ($I = 3$ M $NaClO_4$)	$\log \beta^\circ_{1,n,m}$
$NpO_2^+ + CO_3^{2-} + OH^- \Leftrightarrow NpO_2CO_3OH^{2-}$	7.6 ± 0.3	7.0 ± 0.3
$NpO_2^+ + CO_3^{2-} + 2OH^- \Leftrightarrow NpO_2CO_3(OH)_2^{3-}$	9.56 ± 0.15	7.66 ± 0.15

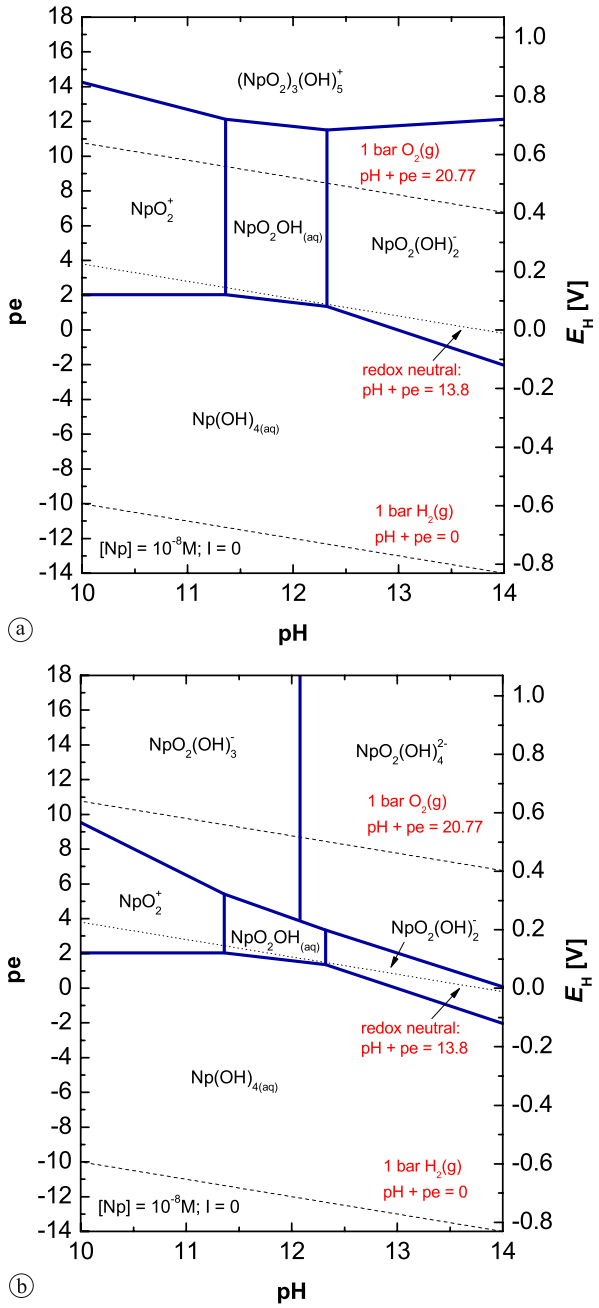

Fig. 2. Predominance diagrams of Np for $-0.8\,\mathrm{V} \le E_\mathrm{H} \le +1\,\mathrm{V}$ and $10 \le \mathrm{pH} \le 14$, (**a**) calculated in accordance with the current thermodynamic data selection of NEA [1]; (**b**) including also hexavalent $NpO_2(OH)_3^-$ and $NpO_2(OH)_4^{2-}$ species as estimated in the present work from its correlation with Z_eff. Only aqueous species considered. Calculations performed with the code Medusa [15].

Little is known about the interaction coefficients of TMA^+ with anionic actinide species. Rao *et al.* [5] estimated $\varepsilon(TMA^+, NpO_2(OH)_2^-)$ by assuming a direct analogy between K^+ and TMA^+. On the other hand, several authors have reported $\varepsilon(TMA^+, X^-)$ as a function of the ionic strength. Data available on $\varepsilon(TMA^+, X^-)(I_\mathrm{m})$ for oxalate (ox), citrate (cit), EDTA, Cl^- and Br^- [16], and carbonate [6] systems have been considered in this work to estimate the magnitude of ε for the anionic Np species forming in the conditions of this study (on average, $I \sim 0.6\,\mathrm{M} = 0.64\,m$). $\varepsilon(TMA^+, X^-)(I = 0.64\,m)$ values calculated for ox^{2-}, Hox^-, cit^{3-}, $Hcit^{2-}$, H_2cit^-, $EDTA^{4-}$, $HEDTA^{3-}$, H_2EDTA^{2-}, H_3EDTA^-, CO_3^{2-}, HCO_3^-, Cl^- and Br^- were found to behave linearly with the charge of the aqueous species ($\varepsilon = -0.40 \times Z - 0.48$, $R^2 = 0.92$, only valid for $I = 0.64\,m$), in line with previous observations compiled for NaCl and $NaClO_4$ systems [14]. These interaction coefficients were used in the SIT equation to calculate $\log^* \beta(I = 0.64\,m)$ for all aqueous species (see Tables A3 and A4 in Sect. A). Although only of qualitative character, this approach is expected to provide more accurate results than the simpler application of the Debye–Hückel equation.

3. Experimental

3.1 Chemicals, E_H and pH measurements

TMA-OH pentahydrate ($\ge$ 97%), TMA-Cl (reagent grade, 97%) and sodium hypochlorite (reagent grade, available chlorine 10–15%) were purchased from Sigma-Aldrich; HCl (Titrisol®), HNO_3 (65%, Suprapur®) and $HClO_4$ (70%, Suprapur®) were purchased from Merck. All solutions were prepared with ultrapure water purified with a Milli-Q-academic (Millipore) apparatus. Before its use, CO_2 was removed by bubbling Ar through the Milli-Q water.

Redox potentials were measured with a Pt combined electrode with Ag/AgCl reference system (Metrohm). An equilibration time of 5 min was considered for the E_H measurement in all samples. Combination pH electrodes (type ROSS, Orion), freshly calibrated against dilute standard pH buffers (pH 1–13, Merck), were used to determine the molal H^+ concentration $[H^+]$. In salt solutions of ionic strength $I \ge 0.1\,\mathrm{mol\,kg^{-1}}$, the measured pH value ($\mathrm{pH_{exp}}$) is an operational apparent value [17, 18], which can be related to $[H^+]$ by:

$$-\log[H^+] = \mathrm{pH_{exp}} + A \qquad (1)$$

A values for the system TMA-Cl were determined under the conditions of this study (0.5–0.7 M TMA-Cl) by measuring $\mathrm{pH_{exp}}$ in the corresponding salt solutions containing known concentrations of HCl (0.002–0.02 M). A values were found to range between 0.05 and 0.10 on the molal scale, and are remarkably small compared to NaCl or $CaCl_2$ solutions of similar ionic strength. Conversion factors to calculate m_i ($\mathrm{mol\,kg^{-1}}$ H_2O) from the molar concentrations c_i ($\mathrm{M} = \mathrm{mol\,L^{-1}}$), as well as the dependence of the water activity a_w with [TMA-Cl] were taken from [6].

3.2 Sample preparation and characterization

All samples were handled and prepared inside an inert gas (Ar) glovebox at $22 \pm 2\,^\circ\mathrm{C}$. Samples were prepared in TMA-(OH, Cl) to avoid the quantitative precipitation of Na-neptunates and retain sufficient Np in solution to allow for X-ray absorption near edge structure (XANES) analysis of Np oxidation state distribution. A solution of 1 M TMA-OH was reacted in three different aliquots with HCl (1 M and 0.01 M) to obtain $-\log[H^+]$ values of $\sim$ 13.5, $\sim$ 12 and $\sim$ 9. Carbonate was ubiquitous in all samples as impurity of TMA-OH (quantified as $4 \pm 1 \times 10^{-3}$ M CO_3^{2-} in 1 M TMA-OH). Because of the dilution effect introduced by the neutralization of TMA-OH with HCl, I and $[CO_3^{2-}]$

varied as 0.5 M $\leq I \leq$ 0.7 M and 2.0×10^{-3} M $\leq [CO_3^{2-}] \leq 2.7 \times 10^{-3}$ M. Three series of samples were prepared, accounting for three different redox conditions: absence of ClO^-, 5×10^{-3} M ClO^- and 5×10^{-2} M ClO^-.

About 2.2 mL of a radiochemically pure and well characterised $^{237}Np(V)$ stock solution 4.6×10^{-2} M were used for the preparation of the samples. The Np(V) redox purity of the stock solution was confirmed by ultraviolet-visible near-infrared spectroscopy (UV-vis/NIR) with a high-resolution UV-vis/NIR spectrometer Cary 5 (Varian, USA). The pH of the stock (originally in 0.1 M HCl) was adjusted to $-\log[H^+] \sim 4$ by addition of 0.01 M TMA-OH to avoid large pH-shifts in the samples after stock addition. The pH adjusted stock was added to the 9 solutions described above to give a final total Np concentration of $\sim 2 \times 10^{-3}$ M in the samples. The pH_{exp} and E_H were measured after the addition of the Np(V) tracer (1–2 h). Typical experimental errors for these parameters are ±0.05 pH-units and ±0.05 V, respectively, although E_H uncertainties for redox-unbuffered samples can increase significantly [19]. The formation of a precipitate was observed in some of the samples after the addition of Np (few minutes to few hours).

After 4 days, samples were centrifuged at 4020 *g* in the Ar glovebox and a UV-vis/NIR spectrum from the supernatant of each sample recorded between 800 nm $\leq \lambda \leq$ 1300 nm. The aqueous concentration of Np was measured after 10 kD ultrafiltration (Pall Life Sciences) at 4 and 7 days by liquid scintillation counting (LSC) with a TriCarb 2500 TR/AB instrument (Canberra-Packard). The detection limit was 5×10^{-9} M for ^{237}Np (α-radiation measured after α/β-discrimination of the counts from the β-emitting daughter nuclide ^{233}Pa).

For solid phase analysis, an aliquot of each solid was washed under Ar-atmosphere in triplicate with ethanol to remove the matrix solution. A first fraction of the resulting solid was dissolved in 2% HNO_3, and neptunium and sodium quantified by LSC and ICP-OES, respectively. A second fraction of the washed solid was characterized by scanning electron microscope-energy disperse spectrometry (SEM-EDS), using a CamScan FE44 SEM equipped with a Noran EDS unit.

3.3 XAFS measurements

XANES/EXAFS spectra were recorded at the INE-Beamline for Actinide Research at ANKA, KIT Campus Nord [20]. The ANKA storage ring was operated at 2.5 GeV electron energy, with a mean electron current of 120 mA. Tuneable monochromatic beam was delivered by the Ge(422) crystal pair in the Lemonnier-type double crystal monochromator (DCM). Higher harmonics were rejected from the two mirrors in the optics of the INE-Beamline and by detuning the second crystal at a constant, controlled 70% from the rocking curve maximum [21].

At least four scans were performed for each Np sample, and the spectra were averaged for XANES/EXAFS data analysis. Spectra were recorded at 22 ± 2 °C in fluorescence mode using a 5-pixel low energy fluorescence Ge solid-state detector (Canberra-Packard Ultra-LEGe, Rüsselsheim, Germany) and Ar-filled ionization chamber to record the incident beam intensity. All spectra were energy calibrated using the first inflection point in the K-edge spectrum of a zirconium metal foil (17 998 eV).

XANES/EXAFS data reduction and analysis were performed with the ATHENA/ARTEMIS package following standard procedures [22]. Structural information was obtained by following a multi-shell approach for EXAFS data fitting. The fit was limited to parameters describing the Np coordination to surrounding oxygen atoms (neighbouring atomic distances (R), EXAFS Debye–Waller factors (σ^2), coordination numbers (N) and relative shift in ionization energy E_0 (ΔE_0)). EXAFS spectra were Fourier transformed (FT) in the k-range between 2–12 $Å^{-1}$ using symmetric square windows.

Theoretical single scattering paths (SS) were calculated with FEFF8.4 [23] using the structure of $Cs_2Np(SO_4)_3(H_2O)_2$ [24] for Np(III/IV) samples and the structure of Np_2O_5 [25] for Np(V) samples. Theoretical SS paths for the fit of Np(VI) samples were calculated using the structure of UO_3 [26], where the central U atom was substituted by Np and paths recalculated using the Atoms routine in Artemis. The amplitude reduction factor (S_0^2) was fixed to 1.0 in all the cases.

3.3.1 Np reference spectra: design and use of a spectro-electrochemical cell

A set of XANES reference spectra was obtained by *in situ* generation of different Np redox states. For this purpose, a spectro-electrochemical cell (based on the design in [27]) was constructed of Plexiglas (poly(methyl methacrylate)) with windows of Kapton® film (polyimide). The cell was designed to allow both transmission and fluorescence mode XAFS, with optical path lengths between the two windows of about 2 cm. The cell was designed with a three-electrode configuration, with both working and counter (or auxiliary) electrodes made of glassy carbon. An Ag/AgCl reference electrode was used in this experiment. Stirring was achieved with a Teflon coated stir bar inside the cell and a magnetically-driven stirrer placed outside the cell. Samples were bubbled with argon during the electrolysis process. A stainless steel outer containment with Kapton® windows was used as second containment, required by beamline regulations for the handling of radioactive material. The spectro-electrochemical cell was connected to a potentiostat (Radiometer analytical, Lyon, France) located in the experimental hutch and operated by the central computer in the beamline control hutch *via* VNC View interface.

A solution of approximately 7 mL of freshly prepared $^{237}Np(V)$ in 1 M $HClO_4$ ($\sim 1 \times 10^{-3}$ M Np) was transferred to the spectro-electrochemical cell. The redox purity of this solution was verified by UV-vis/NIR. The scheme used to obtain different Np redox states was: Np(V) → Np(III) → Np(IV) → Np(VI). A potential of −300 mV was first applied to the Np(V) solution to obtain Np(III) (~ 14 h). After the reduction of Np(V) to Np(III), oxidizing potentials were applied: +200 mV to obtain Np(IV) (~ 7 h) and subsequently +1000 mV for Np(VI) (~ 18 h). During the whole electrochemical processes, Np L_{III}-edge (17 610 eV) XANES measurements were performed *in situ* to monitor the Np oxidation state(s). EXAFS signal recording began

only after exhaustive electrolysis for every valence indicated by coulometry and reproducibility of XANES spectra. The total electrolysis time was previously estimated by an *ex-situ* experiment under identical conditions.

3.3.2 Np in TMA-(OH, Cl) solutions

All Np samples in TMA-(OH, Cl) for synchrotron measurements were prepared in 400 µL polyethylene vials. In the case of solid samples, a suspension containing 1–2 mg of material was transferred to the vial and centrifuged for 10 min at 4020 *g*. The centrifuge vials were then mounted in a gas-tight cell inside the Ar-glovebox and transported to the INE-Beamline. The design of this cell was conceptually the same as for the spectro-electrochemical cell described in Sect. 3.3.1, but with no inserts for the mounting of the electrodes. A continuous flow of Ar was flushed through the cell during the synchrotron measurements to ensure inert gas atmosphere.

4. Results and discussion

4.1 Wet chemistry and UV-vis/NIR

Fig. 3 summarizes $-\log[H^+]$ and E_H measurements for all samples, plotted in the predominance diagram of Np for $8 \leq -\log[H^+] \leq 14$ and $-0.8\,V \leq E_H \leq +1\,V$. The diagram was calculated in accordance with the thermodynamic data base (TDB) and experimental conditions described in Sects. 2 and 3, respectively. The identification names allocated to the samples studied (Np-1 through Np-9) are indicated in the figure.

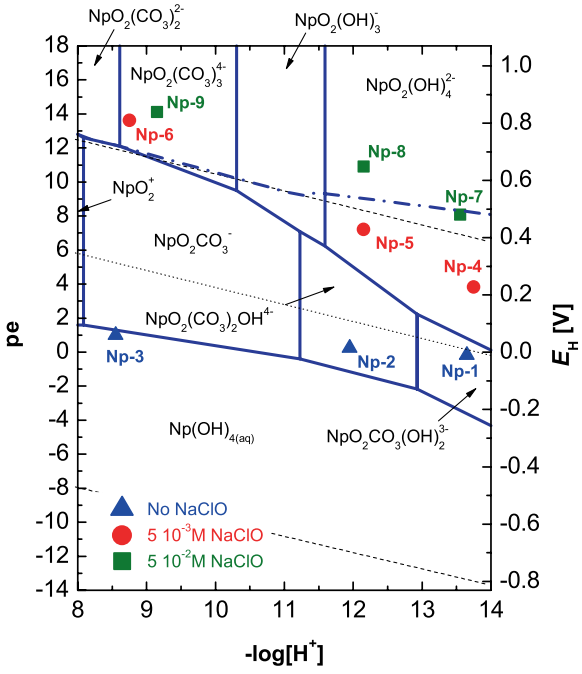

Fig. 3. Predominance diagram of Np aqueous species, including experimental $-\log[H^+]$ and E_H measurements. Calculations done with Np TDB described in Sect. 2, considering $[Np]_{tot} = 1 \times 10^{-4}$ M ($1.1 \times 10^{-4}\,m$); $[CO_3^{2-}]_{tot} = 2.35 \times 10^{-3}$ M ($2.5 \times 10^{-3}\,m$); $I = 0.6$ M ($0.64\,m$). I corrections by SIT as described in Sect. 2. Thick dashed line: border Np(V)/Np(VI) for the conditions of this study, as calculated with the NEA-TDB [1].

Significantly different E_H values were determined for samples in 5×10^{-3} M ClO^- and 5×10^{-2} M ClO^-. These differences were caused not only by the different ClO^- initial concentrations, but also by the significant proportion of ClO^- consumed in the lower concentration solution upon Np(V) oxidation ($[Np]_{tot} = 2 \times 10^{-3}$ M).

As shown in Fig. 3, sample Np-3 falls within the stability field of Np(V) and Np(IV). The E_H measured for samples Np-1 to Np-3 must be considered uncertain, because they were not redox buffered and the equilibration time (5 min) was probably not sufficient to obtain stable and reliable E_H readings. Despite the qualitative character of the diagram, Fig. 3 shows that predominance of Np(VI) aqueous species can be expected for samples Np-4 to Np-9.

The concentration of Np in the supernatant determined by LSC after 10 kD ultrafiltration and the visual description of the solid phases formed are given in Table 3, together with $-\log[H^+]$, E_H and the ratio Np : Na determined for the solid phases by chemical analysis and SEM-EDS. As shown in the table, a very different behaviour was observed in the absence (samples Np-1 to Np-3) and presence of ClO^- (samples Np-4 to Np-9). Two types of solids were found to form: the greenish solid phase precipitating in the absence of ClO^- was likely $Np^{V}O_2OH(s)$ while the brownish-purple phase corresponded to $Np^{VI}O_3 \cdot xH_2O(s)$ or a Na-Np(VI) phase, considering the colour expected for Np(VI) (purple, see Sect. 4.2 and [28]) as well as spectroscopic observations discussed below.

In the presence of ClO^-, only the samples at $-\log[H^+] \sim 13.5$ show the complete solubilization of Np. This behaviour, different from observations made for Np(V) under the same conditions but absence of ClO^- (sample Np-1), indicates the formation of anionic Np(VI) hydroxide species, in agreement with thermodynamic calculations shown in Fig. 3.

UV-vis/NIR spectra were obtained for the supernatant of samples Np-1 to Np-9. Clear features were observed for samples without ClO^- (Fig. 4). Hence, sample Np-3 shows peaks unequivocally identified as NpO_2^+ ($\lambda = 980$ nm) and $NpO_2CO_3^-$ ($\lambda = 991$ nm). The feature observed in sample Np-1 within 980 nm $\leq \lambda \leq$ 1080 nm indicates the presence of at least two species. Within the same NIR region, Neck *et al.* [13] observed the formation of several Np(V)-OH-CO_3 species with well-defined spectroscopic features, namely $NpO_2(CO_3)_2OH^{4-}$ ($\lambda = 1010$ nm) and $NpO_2CO_3(OH)_2^{3-}$ ($\lambda = 1020$–1025 nm). Features corresponding to these species were characterized by significantly large full width at half maximum (FWHM = 20 nm and 30 nm, respectively) compared to NpO_2^+ (FWHM = 7 nm). A third feature observed in [13] at $\lambda = 1050$ nm was ascribed to colloidal Np(V), whereas a peak "shoulder" at $\lambda = 1035$ nm remained unidentified but likely corresponded to an additional Np(V)-OH-CO_3 species. This comparison strongly suggests the predominance of $(NpO_2)_x(CO_3)_y(OH)_z^{x-2y-z}$ species in sample Np-1, although no unequivocal identification of each individual species can be drawn because of the broadness and overlapping of their corresponding peaks, as well as slight deviations in peak position potentially arising from differences in the matrix solution (3 M $NaClO_4$ in [13] and ~ 0.7 M TMA-(OH, Cl) in our study).

Table 3. Concentration of Np in the supernatant, $-\log[H^+]$ and E_H for samples Np-1 to Np-9 (after ultrafiltration) at $t = 7$ days. In case of solid phase formation, visual description and ratio Np : Na provided.

Sample	$-\log[H^+]$	E_H [V]	[Np] [*m*]	Solid phase	Np : Na in solid (chem. anal. // SEM-EDS)
Np-1	13.65	−0.010	1.76×10^{-4}	Yes, greenish	Not measured
Np-2	11.95	0.014	4.34×10^{-5}	Yes, greenish	1 : 0.02 // n.m.
Np-3	8.55	0.059	1.45×10^{-3}	No	
Np-4	13.75	0.226	1.86×10^{-3}	No	
Np-5	12.15	0.427	3.00×10^{-4}	Yes, brownish-purple	1 : 0.02 // 1 : 0.04
Np-6	8.75	0.805	1.09×10^{-4}	Yes, brownish-greenish	1 : 0.04 // 1 : 0.05
Np-7	13.55	0.478	1.82×10^{-3}	No	
Np-8	12.15	0.646	8.77×10^{-6}	Yes, brownish-purple	1 : 0.77 // 1 : 0.66
Np-9	9.15	0.835	1.74×10^{-5}	Yes, brownish-purple	1 : 0.13 // 1 : 0.12

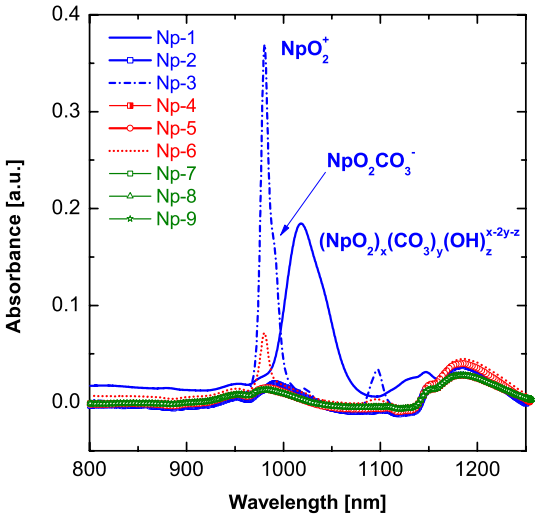

Fig. 4. UV-vis/NIR spectra of supernatant solutions from samples Np-1 to Np-9. Wavelengths for Np(V) species as reported in [13].

No NIR features were observed within 800 nm $\leq \lambda \leq$ 1300 nm for samples Np-4, Np-5, Np-7, Np-8 and Np-9, despite the high Np concentration in some of these samples ($\sim 2 \times 10^{-3}$ M in Np-4 and Np-7). This result supports the argument that none of the Np(V) species observed in samples Np-1 to Np-3 exist in the presence of ClO^-. We postulate that the formation of (centro-)symmetric species (*e.g.*, $NpO_2(OH)_4^{2-}$) and the resulting forbidden f-f transitions have led to a significant decrease of the extinction coefficients (ε) for Np(VI) species under the given conditions.

A small peak at $\lambda = 980$ nm (corresponding to NpO_2^+) was observed in the NIR of sample Np-6. The concentration of NpO_2^+ calculated from this feature was significantly lower than the total Np concentration determined after ultrafiltration of this sample, thus indicating the presence of additional species. In line with the thermodynamic calculations and the experimental $-\log[H^+]$ and E_H values shown in Fig. 3, the presence of the species $NpO_2(CO_3)_3^{4-}$ is to be expected, resulting in an aqueous mixture of Np(V) and Np(VI) in sample Np-6.

4.2 XAFS measurements

4.2.1 Np XANES/EXAFS reference data in $HClO_4$

The Np L_{III}-edge XANES spectra recorded for the four different redox species (states) obtained by electrolysis are shown in Fig. 5. The energy at the inflection point and white line (maxima) of the Np L_{III}-edge, as well as the colour of each redox state solution are summarized in Table 4.

As shown in Table 4, the differences in energy position of the white line as a measure of E_0 relative to the white line maximum of Np(V) (17 614.0 eV) are approximately −3 eV, +1 eV and +2 eV for Np(III), Np(IV) and Np(VI), respectively. The energy position of Np(IV) with respect to Np(V) is in reverse order of the expected increase in E_0 with increasing valence state of the absorbing atom. Similar observations have also been reported for U, Np and Pu [29–32]. Other characteristic features of the Np L_{III} XANES spectra in Fig. 5 involve trends in intensities. Np(III) and Np(IV) have intense white lines, whereas the white line intensities in the Np(V) and Np(VI) XANES are comparatively reduced. These neptunyl cations also exhibit shoulders on the high energy side of their white lines, which are attributed to multiple scattering (MS) from the linear O=Np=O moiety [33] and therefore are absent for Np(III) and Np(IV).

According to these spectroscopic features, one might conclude that the combined use of the energy position of

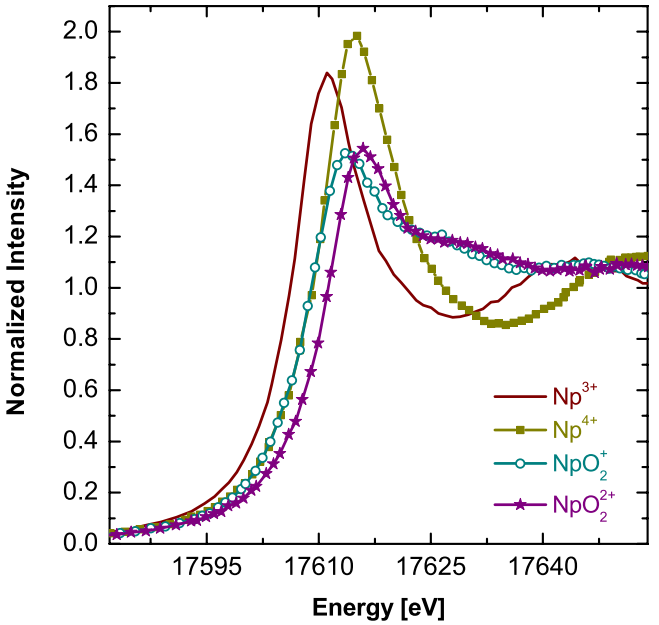

Fig. 5. XANES reference spectra for Np^{3+}, Np^{4+}, NpO_2^+ and NpO_2^{2+}, as obtained electrochemically in 1 M $HClO_4$. All spectra normalized and corrected in energy *vs.* K-edge of Zr.

Table 4. Energies at the inflection point and white line for XANES reference spectra, as well as for aqueous and solid samples in TMA-(OH, Cl) solutions, after energy calibration and normalization. Last column reporting the colour of each endpoint solution (reference samples) or redox state proposed by comparison with reference data (unknown samples).

Sample	Inflection point [eV]	White line [eV]	Colour/ redox state
Np^{3+}/reference	17 607.5	17 611.3	Red-brown
Np^{4+}/reference	17 610.8	17 614.9	Green
NpO_2^+/reference	17 609.1	17 614.0	Turquoise
NpO_2^{2+}/reference	17 611.7	17 616.0	Purple
Np-1/aqueous	17 608.7	17 614.2	+V
Np-3/aqueous	17 608.4	17 612.4	+V
Np-4/aqueous	17 610.7	17 616.9	+VI
Np-5/aqueous	17 609.9	17 616.6	+VI
Np-7/aqueous	17 610.2	17 617.5	+VI
Np-6/aqueous	17 609.9	17 614.7	+V and +VI
Np-1/solid	17 607.4	17 612.7	+V
Np-2/solid	17 607.9	17 612.7	+V
Np-5/solid	17 609.3	17 615.5	+VI
Np-8/solid	17 610.2	17 616.6	+VI

E_0 and the shape of the XANES edge is sufficient to distinguish between different redox states of Np in solution. For valence mixtures or for samples involving different phases (*e.g.*, aqueous and solid), however, this approach needs to be verified. As demonstrated by Denecke *et al.* for Np(IV) [32], the white line intensity generally varies not only with valence but also with the degree of condensation of the sample.

The structural parameters obtained from curve fitting of the k^3-weighted EXAFS spectra recorded for Np(III), Np(IV) and Np(VI) are summarized in Table 5. Data reported by other authors in acidic conditions have been included in the table for comparison.

The EXAFS of Np(III) and Np(IV) are composed of a single oscillation, giving rise to a single FT peak at $R + \Delta R \sim 2$ Å and about 1.9 Å, respectively. The best curve fit for the Np(III) spectrum yields $R = 2.51$ Å and $N = 9$, corresponding to a hydration number of nine. Np(IV) is found to be surrounded by 10 coordinating water molecules at a distance of 2.38 Å. These distances are in good agreement with those reported in the literature.

Although little ambiguity exists in the Np-O bond length interpretation, the hydration numbers of Np^{3+} and Np^{4+} ions are still a matter of discussion. Generally, EXAFS suffers from relatively large errors in the coordination numbers (±10–20%). Our Np(III) hydration number of nine seems plausible, although it is one water molecule greater than predictions available from density functional theory (DFT) ($N = 8$–9, [27]). We found a $N(H_2O)$ value of 10 for the Np^{4+} ion, identical to that reported by Ikeda-Ohno and co-authors in their *ex situ* EXAFS study on Np complexation behaviour [28].

Np(VI), in contrast, shows a more intricate oscillation pattern, and its FT shows several significant peaks. The intense FT peaks at $R + \Delta R \sim 1.4$ Å arises from SS of the photoelectron on the axial O atoms (O_{ax}) and is, hence, a representative indicator of the neptunyl (NpO_2^{n+}) unit. A less intense peak at $R + \Delta R \sim 2$ Å is attributed to the SS on the O atoms of coordinated water molecules in the neptunyl equatorial plane ($O_{eq}(H_2O)$). The other further distant FT peaks are not included in the curve fitting model. The curve fit results reveal that Np(VI) is coordinated by two O_{ax} atoms at a distance of 1.75 Å and by five $O_{eq}(H_2O)$ at 2.41 Å, consistent with literature data (see Table 1). Therefore, the Np(VI) aquo species can probably be written as $[NpO_2(H_2O)_5]^{2+}$, similar to those reported for U(VI) and Pu(VI) [35, 36].

Our *in situ* EXAFS results using the spectro-electrochemical cell show that the coordination environment of Np(III), Np(IV) and Np(VI) species determined in $HClO_4$ is in good agreement with most literature data. These EXAFS results further prove that XANES measurements of the final Np species generated after exhaustive bulk electrolysis were the actual pure Np species with well defined redox states.

Table 5. Structural parameters determined for Np^{3+}, Np^{4+} and NpO_2^{2+} aqueous species, as prepared by in situ electrolysis (1 M $HClO_4$). Amplitude reduction factor (S_0^2) fixed to 1.0. Data reported by other authors for speciation studies under acidic conditions included for comparison.

Sample	Shell	N	R [Å]	σ^2 [Å^2]	ΔE_0 [eV]	R-factor	Reference
$Np^{3+} \cdot nH_2O$	O	9 ± 1	2.51 ± 0.02	0.009 ± 0.003	11 ± 1	0.003	This study
		10.0 ± 1.2	2.51 ± 0.01	0.009 ± 0.001	7.2 ± 1.1	0.002	[34][a]
		9 ± 1	2.48 ± 0.02	0.012 ± 0.003	1.8	–	[27][b]
$Np^{4+} \cdot n'H_2O$	O	10 ± 1	2.38 ± 0.01	0.007 ± 0.002	12 ± 1	0.001	This study
		10.4 ± 1.0	2.40 ± 0.01	–	–	–	[28][b]
		9 ± 1	2.37 ± 0.02	0.007 ± 0.002	6.7	–	[27][b]
$NpO_2^{2+} \cdot n''H_2O$	O_{ax}	2*	1.75 ± 0.01	0.001 ± 0.001	13 ± 2	0.014	This study
		2*	1.76 ± 0.01	–	–	–	[28][b]
		2*	1.73 ± 0.02	0.002 ± 0.001	9.8	–	[27][b]
	O_{eq}	5*	2.41 ± 0.03	0.008 ± 0.002			This study
		5.3 ± 0.5	2.42 ± 0.01	–			[28][b]
		5 ± 1	2.36 ± 0.03	0.006 ± 0.004			[27][b]

* Parameters fixed in the fit; a: In 1 M HCl; b: In 1 M $HClO_4$.

4.2.2 XANES of Np aqueous species in TMA-(OH, Cl)

XANES spectra of aqueous samples Np-1, Np-3, Np-4, Np-5 and Np-7 are shown in Fig. 6a. Two groups of samples with a well defined difference in energies for the Np L_{III}-edge can be identified, which compare generally well with XANES reference spectra described in Sect. 4.2.1 for Np(V) and Np(VI). Both groups exhibit a reduced white line intensity and the MS feature characteristic for the "yl" cation. The observed differences in energy at the inflection point and white line (Table 4) allow the identification of the redox state based on XANES spectra. Differences between reference and sample spectra (*e.g.*, lower inflection point energies) likely reflect differences in their aqueous speciation. However, the absolute difference in energy for the inflection point and white line of the Np(V) and Np(VI) sample spectra is similar to that observed for the reference data.

Energy values determined for inflection point and white line of sample Np-6 (spectrum not shown) lay in between those determined for Np(V) and Np(VI) references (Table 4). This observation probably indicates the presence of a mixture of Np(V) and Np(VI) redox states, in line with results obtained by UV-vis/NIR. The XANES spectrum of sample Np-6 was successfully reproduced by linear combination of Np(V) and Np(VI) spectra, with significant contributions of both redox states (> 40%).

The neptunium redox distribution determined by XANES for aqueous samples is in very good agreement with the Np(V/VI) redox border calculated including the species $NpO_2(OH)_3^-$ and $NpO_2(OH)_4^{2-}$, confirming the stability of Np(VI) aqueous species even under mildly oxidizing conditions. The slight disagreement of experimental observations with thermodynamic calculations for sample Np-6 could be attributed to inaccuracies in the estimated $\varepsilon(TMA^+, X^-)$ for a highly charged species such as $NpO_2(CO_3)_3^{4-}$. Due to the relatively weak pH-buffering capacity of this sample ($-\log[H^+] \sim 8.7$), a larger uncertainty could also be considered for the measured pH_{exp}.

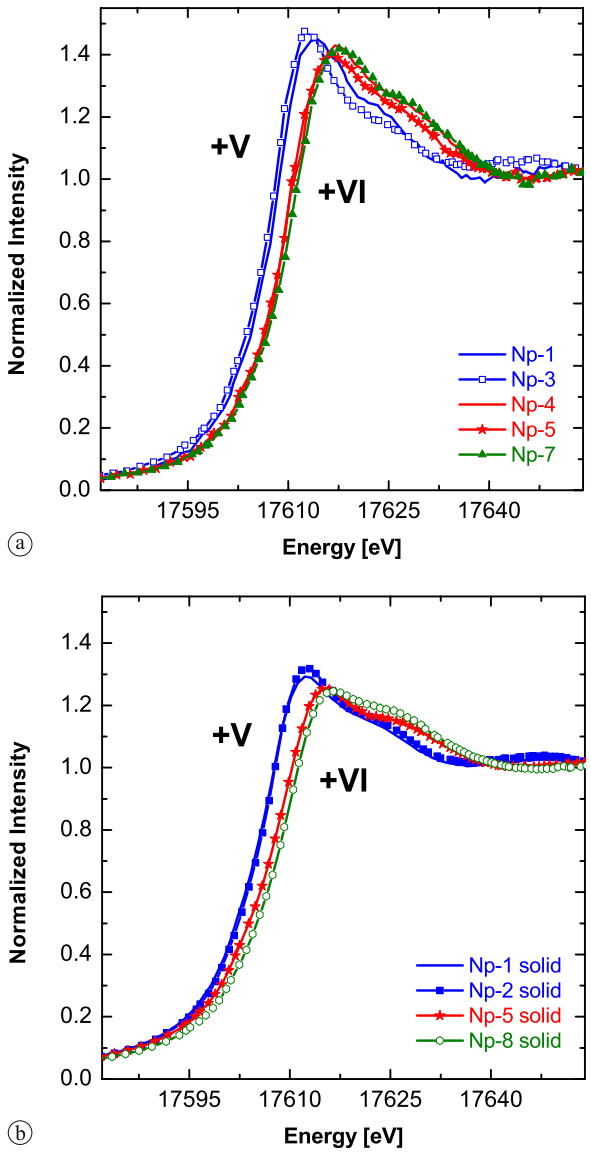

Fig. 6. Experimental Np L_{III} XANES spectra: (**a**) for aqueous supernatant of samples Np-1, Np-3, Np-4, Np-5 and Np-7, (**b**) for solid phases of samples Np-1, Np-2, Np-5 and Np-8.

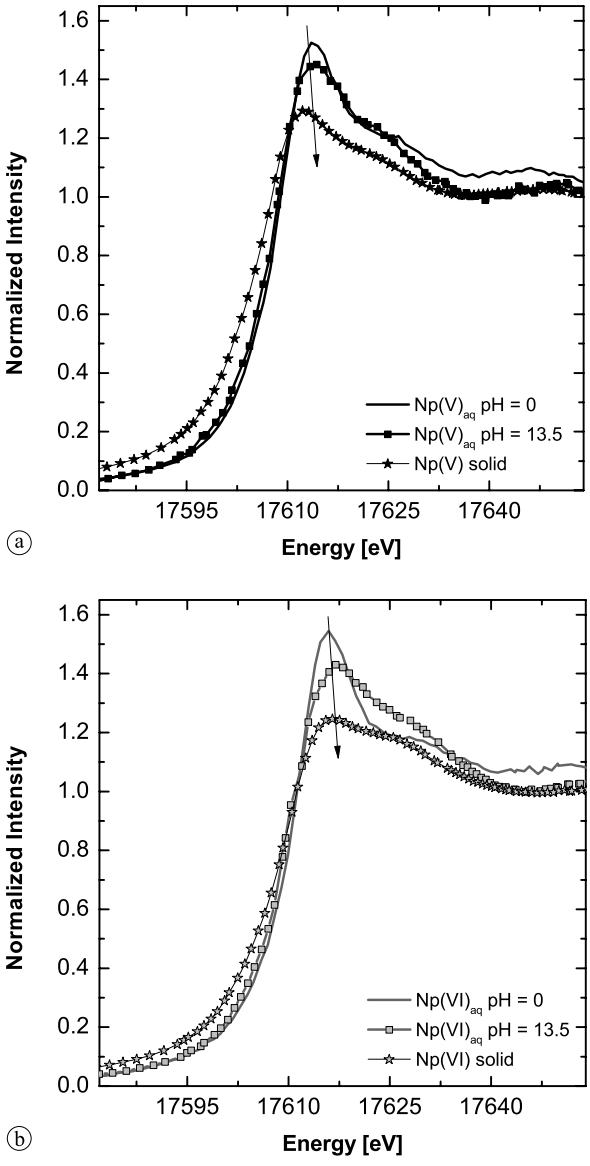

Fig. 7. Comparison of Np L_{III} XANES spectra for aqueous Np species forming in acidic and alkaline conditions, as well as for solids: (**a**) Np(V), (**b**) Np(VI).

Table 6. Structural parameters determined for Np(V/VI) solids prepared in TMA-(OH, Cl) solutions. Amplitude reduction factor (S_0^2) fixed to 1.0.

Sample	Shell	N	R [Å]	σ^2 [Å^2]	ΔE_0 [eV]	R-factor
Np-1	O_{ax}	2*	1.86 ± 0.01	0.005 ± 0.001	5 ± 3	0.004
	O_{eq1}	2*	2.23 ± 0.03	0.007 ± 0.005		
	O_{eq2}	3*	2.42 ± 0.03	0.005 ± 0.003		
Np-2	O_{ax}	2*	1.87 ± 0.02	0.007 ± 0.004	5*	0.004
	O_{eq1}	2*	2.24 ± 0.03	0.003 ± 0.006		
	O_{eq2}	3*	2.43 ± 0.02	0.002 ± 0.004		
Np-5	O_{ax}	2*	1.80 ± 0.02	0.010 ± 0.003	−6 ± 7	0.002
	O_{eq}	4*	2.18 ± 0.04	0.007 ± 0.003		
Np-9	O_{ax}	2*	1.79 ± 0.01	0.005 ± 0.001	11 ± 3	0.011
	O_{eq}	5*	2.25 ± 0.03	0.025 ± 0.004		

* Parameters fixed in the fit.

4.2.3 XANES-EXAFS of Np solid phases in TMA-(OH, Cl)

XANES spectra of solid samples Np-1, Np-2, Np-5 and Np-8 are shown in Fig. 6b. As for the aqueous species, two groups can be clearly identified based on the XANES spectra of the solid phases (Table 4). These groups show moderate agreement with Np(V) and Np(VI) data (both for inflection point and white line) determined for the aqueous samples (both in $HClO_4$ and TMA-(OH, Cl) solutions). A significantly lower intensity of the white line was obtained for the solid phases compared to the aqueous species (Fig. 7), in agreement with previous experimental observations available for Np(IV) samples [32]. This decrease is the main reason for the differences with the aqueous species in terms of energies for inflection point, confirming the need of XANES reference spectra in different condensation states (aqueous and solid phases) to accurately characterize redox states.

Experimental and theoretical k^3-weighted Np L_{III}-edge EXAFS spectra and their corresponding Fourier transforms are shown in Fig. 8. Structural parameters resulting from the fits are listed in Table 6. Distances obtained for Np−O_{ax} and Np−O_{eq} for the solid samples Np-1 and Np-2 are in agreement with those expected for a Np(V) oxy-hydroxide. Although not resolved in the FT diagram, the best fit for both samples was obtained when defining two types of O_{eq}. Different combinations were evaluated in the fit ($1O_{eq\text{-}short} + 4O_{eq\text{-}long}$, $2O_{eq\text{-}short} + 3O_{eq\text{-}long}$, $3O_{eq\text{-}short} + 2O_{eq\text{-}long}$), with the option $2O_{eq\text{-}short} + 3O_{eq\text{-}long}$ providing the lowest R-factor (Table 6). In all cases, however, the average Np−O_{eq} distance was 2.34–2.35 Å. This distance is significantly shorter than the distance Np(V)−O_{eq} expected for a pure oxide ($r_{NpO_2^+} + r_{O^{2-}} = 1.12$ [9] + 1.40 [37] = 2.52 Å) but is very close to the distance predicted for a hydroxide ($r_{NpO_2^+} + r_{OH^-} = 1.12 + 1.22^{\#} = 2.34$ Å), in agreement with the hydrous fresh precipitate expected under the conditions of this study.

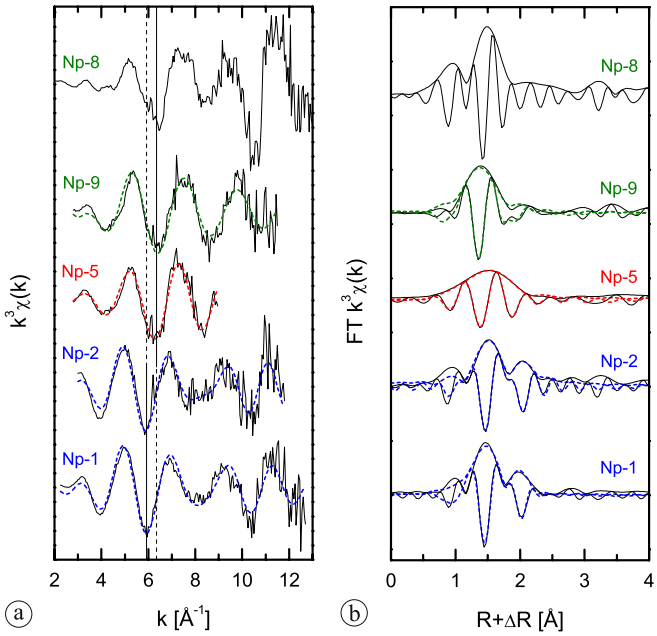

Fig. 8. (**a**) Experimental and theoretical k^3-weighted Np L_{III}-edge EXAFS spectra, and (**b**) Fourier transforms (modulus and imaginary parts) for solid phases in samples Np-1, Np-2, Np-5, Np-8 and Np-9. Solid and dashed vertical lines highlight differences between EXAFS spectra of Np(V) and Np(VI) solid samples.

Significantly shorter Np−O_{ax} and Np−O_{eq} distances were observed for samples Np-5 and Np-9, clearly indicating the predominance of Np(VI). Np−O_{ax} distances in these samples are slightly longer (0.03 to 0.06 Å) than those determined for the NpO_2^{2+} aquo ion in $HClO_4$ (Table 5), which is consistent with the shorter Np−O_{eq} distances also obtained: a general inverse relationship between O_{ax} and O_{eq} bond lengths is often observed. Np−O_{ax} and Np−O_{eq} dis-

[#] r_{OH^-} calculated from $Np^{VI}O_2(OH)_4^{2-}$, Np^{IV}-OH-fulvic, $U^{VI}O_2(OH)_4^{2-}$ and $[Co(NH_3)_6]_2[U^{VI}O_2(OH)_4]_3 \cdot 2H_2O$, according to $r_{OH^-} = d_{M^{n+}-OH^-} - r_{M^{n+}}$

– $Np^{VI}O_2(OH)_4^{2-}$. $d_{M^{n+}-OH^-} = 2.21$ Å [8]; $r_{NpO_2^{2+}} = 1.01$ Å [p.w.]; $r_{OH^-} = 1.20$ Å.

– Np^{IV}-OH-fulvic. $d_{M^{n+}-OH^-} = 2.25$ Å [38]; $r_{Np^{4+}} = 1.02$ Å [9]; $r_{OH^-} = 1.23$ Å.

– $U^{VI}O_2(OH)_4^{2-}$. $d_{M^{n+}-OH^-} = 2.26$ Å [39]; $r_{UO_2^{2+}} = 1.04$ Å [8]; $r_{OH^-} = 1.22$ Å.

– $[Co(NH_3)_6]_2[U^{VI}O_2(OH)_4]_3 \cdot 2H_2O$. $d_{M^{n+}-OH^-} = 2.26$ Å [40]; $r_{UO_2^{2+}} = 1.04$ Å [8]; $r_{OH^-} = 1.22$ Å.

tances determined for Np(VI) solid phases agree well with data reported in [8] for the aqueous $NpO_2(OH)_4^{2-}$ (1.82 ± 0.02 Å and 2.21 ± 0.03 Å, respectively), indicative again of the hydrous character of the fresh precipitate formed. Differences in coordination number between samples Np-5 and Np-9 could be attributed to the presence of different solid structures, although the high uncertainties associated to this parameter in EXAFS fitting do not allow conclusive interpretations to be provided.

EXAFS spectrum and FT of sample Np-8 confirmed the predominance of Np(VI). However, no satisfactory multishell EXAFS fits were obtained for this sample. This could be explained by the presence of a mixture of solids (*i.e.* $Np^{VI}O_3 \cdot H_2O$ and $Na_2Np^{VI}{}_2O_7$). On the other hand, the feature at $R + \Delta R \sim 3.2$ Å could be fit reasonably well with Na as backscatter. This observation is in line with the chemical analysis reported in Table 3. SEM-EDS analysis of this sample did not indicate the presence of Cl (as ClO^-) in the solid structure and confirmed its higher Na content compared with other samples. A further indication of the presence of a mixture of solids in sample Np-8 can be extracted from the Np aqueous concentrations reported in Table 3. Assuming the predominance of the aqueous species $NpO_2(OH)_4^{2-}$ in the $-\log[H^+]$ range 12 to 14, slopes of 2 and 1 would be expected for Np solubility curves controlled by $Np^{VI}O_3 \cdot H_2O$ and $Na_2Np^{VI}{}_2O_7$, respectively ($Np^{VI}O_3 \cdot H_2O + 2OH^- \Leftrightarrow NpO_2(OH)_4^{2-}$; $0.5Na_2Np^{VI}{}_2O_7 + 1.5H_2O + OH^- \Leftrightarrow Na^+ + NpO_2(OH)_4^{2-}$). Although acknowledging the large uncertainty affecting the experimental measurement of $-\log[H^+] \sim 13.5$ in TMA-(OH, Cl) solutions, the slope resulting from an hypothetical solubility curve traced between samples Np-7 and Np-8 is ~ 1.6, laying in between slopes expected for $Np^{VI}O_3 \cdot H_2O$ and $Na_2Np^{VI}{}_2O_7$ solid phases.

Altogether, EXAFS results presented in this section confirm the Np redox distribution determined by XANES.

5. Summary and conclusions

XANES reference spectra obtained for aqueous Np(III/IV/V/VI) in 1 M $HClO_4$ were used to identify aqueous Np(V/VI) species forming in alkaline TMA-(OH, Cl) solutions. XANES spectra of condensed samples (solid phases) suffer from a significant decrease in the white line intensity, but relative differences in energy between Np(V/VI) XANES spectra are retained.

Wet chemistry and spectroscopic data of Np in alkaline TMA-(OH, Cl) solutions confirm the stability and relevance of Np(VI) aqueous species and solid compounds in hyperalkaline systems even under mildly oxidizing conditions. For aqueous species, these observations are further supported by correlations of literature thermodynamic data for actinides (U, Np, Pu and Am). Thermodynamic calculations performed considering these correlations predict the formation of anionic Np(VI) hydrolysis species under oxic conditions, analogous to those already described for U(VI).

EXAFS results also point towards a Na-neptunate(VI) solid formation at [Na] = 0.01 M, which indicates the potential relevance of Na-Np(VI) (and Ca-Np(VI)) solid phases in cementitious and $NaCl/CaCl_2$-dominated saline environments.

Appendix

Table A1. Comparison of water activities in various background electrolytes (NaCl, $NaClO_4$, NH_4Cl and TMA-Cl) at 298.15 K.

C [M]	NaCl [1]	$NaClO_4$ [1]	NH_4Cl [1]	TMA-Cl [6]
0.10	0.9966	0.9966	0.9966	0.9964
0.50	0.9833	0.9833	0.9836	0.9819
1.00	0.9661	0.9660	0.9669	0.9635
2.00	0.9284	0.9279	0.9311	0.9254
3.00	0.8850	0.8840	0.8918	0.8862
4.00	0.8352	0.8331	0.8491	0.8460

Table A2. Factors ρ for the conversion of molarity (c_i) to molality (m_i) of a substance B, in various background electrolytes (NaCl, $NaClO_4$, NH_4Cl and TMA-Cl) at 298.15 K.

C [M]	ρ (NaCl) [1]	ρ ($NaClO_4$) [1]	ρ (NH_4Cl) [1]	ρ (TMA-Cl) [6]
0.10	1.0046	1.0075	1.0066	1.0110
0.50	1.0118	1.0265	1.0219	1.0571
1.00	1.0215	1.0515	1.0420	1.1206
2.00	1.0429	1.1062	1.0855	1.2724
3.00	1.0668	1.1678	1.1339	1.4698
4.00	1.0930	1.2374	1.1877	1.7367

Table A3. SIT ion interaction coefficients considered for all aqueous species of interest in this work. $\varepsilon(i, TMA^+)$ estimated for $I = 0.64\,m$.

i	j	$\varepsilon(i, j)$ [mol kg^{-1}]	Reference
H^+	Cl^-	0.12	[1]
OH^-	TMA^+	−0.07	Estimated by correlation with Z at $I = 0.64\,m$ [p.w.][a]
HCO_3^-	TMA^+	−0.17	Value at $I = 0.64\,m$ determined from $\varepsilon(I_m)$ provided in [6]
CO_3^{2-}	TMA^+	0.49	Value at $I = 0.64\,m$ determined from $\varepsilon(I_m)$ provided in [6]
Np^{4+}	Cl^-	0.35	Estimated by correlation with Z according with [14][b]
$Np(OH)_4(aq)$	TMA^+, Cl^-	0	By definition (in SIT)
NpO_2^+	Cl^-	0.09	[1]
$NpO_2OH(aq)$	TMA^+, Cl^-	0	By definition (in SIT)
$NpO_2(OH)_2^-$	TMA^+	−0.07	Estimated by correlation with Z at $I = 0.64\,m$ [p.w.][a]
	TMA^+	−0.01	Analogy with K^+ [5]
$NpO_2CO_3^-$	TMA^+	−0.07	Estimated by correlation with Z at $I = 0.64\,m$ [p.w.][a]
$NpO_2(CO_3)_2^{3-}$	TMA^+	0.71	Estimated by correlation with Z at $I = 0.64\,m$ [p.w.][a]
$NpO_2(CO_3)_3^{5-}$	TMA^+	1.49	Estimated by correlation with Z at $I = 0.64\,m$ [p.w.][a]
$NpO_2CO_3OH^{2-}$	TMA^+	0.32	Estimated by correlation with Z at $I = 0.64\,m$ [p.w.][a]
$NpO_2CO_3(OH)_2^{3-}$	TMA^+	0.71	Estimated by correlation with Z at $I = 0.64\,m$ [p.w.][a]
$NpO_2(CO_3)_2OH^{4-}$	TMA^+	1.10	Estimated by correlation with Z at $I = 0.64\,m$ [p.w.][a]
NpO_2^{2+}	Cl^-	0.15	Estimated by correlation with Z according with [14][b]
NpO_2OH^+	Cl^-	0.05	Estimated by correlation with Z according with [14][b]
$(NpO_2)_2(OH)_2^{2+}$	Cl^-	0.69	Analogy with U(VI)
$(NpO_2)_3(OH)_5^+$	Cl^-	0.81	Analogy with U(VI)
$NpO_2(OH)_2(aq)$	TMA^+, Cl^-	0	By definition (in SIT)
$NpO_2(OH)_3^-$	TMA^+	−0.07	Estimated by correlation with Z at $I = 0.64\,m$ [p.w.][a]
$NpO_2(OH)_4^{2-}$	TMA^+	0.32	Estimated by correlation with Z at $I = 0.64\,m$ [p.w.][a]
$NpO_2CO_3(aq)$	TMA^+, Cl^-	0	By definition (in SIT)
$NpO_2(CO_3)_2^{2-}$	TMA^+	0.32	Estimated by correlation with Z at $I = 0.64\,m$ [p.w.][a]
$NpO_2(CO_3)_3^{4-}$	TMA^+	1.10	Estimated by correlation with Z at $I = 0.64\,m$ [p.w.][a]
$(NpO_2)_2CO_3(OH)_3^-$	TMA^+	−0.07	Estimated by correlation with Z at $I = 0.64\,m$ [p.w.][a]

a: $\varepsilon(TMA^+, X^-) = -0.40 \times Z - 0.48$; b: $\varepsilon(M^+, Cl^-) = 0.10 \times Z - 0.05$.

Table A4. Equilibrium constants ($I = 0$, 298.15 K) and SIT model parameters used to describe the ionic strength dependence in TMA-Cl solutions.

Reaction	$\log^* \beta^\circ$	Reference	Δz^2	$\Delta\varepsilon(i, j)$ [mol kg^{-1}]
$H_2O \Leftrightarrow H^+ + OH^-$	−14	[1]	2	0.05
$0.5H_2O \Leftrightarrow H^+ + e^- + 0.25O_2(g)$	−20.77	[1]	1	0.12
$H^+ + e^- \Leftrightarrow 0.5H_2(g)$	0	[1]	−1	−0.12
$CO_3^{2-} + H^+ \Leftrightarrow HCO_3^-$	10.33	[1]	−4	−0.78
$NpO_2^+ + 4H^+ + e^- \Leftrightarrow Np^{4+} + 2H_2O$	10.21	[1]	11	−0.22
$Np^{4+} + 4H_2O \Leftrightarrow Np(OH)_4(aq) + 4H^+$	−8.3	[1]	−12	0.13
$NpO_2^{2+} + e^- \Leftrightarrow NpO_2^+$	19.59	[1]	−3	−0.06
$NpO_2^+ + H_2O \Leftrightarrow NpO_2OH(aq) + H^+$	−11.3	[1]	0	0.03
$NpO_2^+ + 2H_2O \Leftrightarrow NpO_2(OH)_2^- + 2H^+$	−23.6	[1]	2	0.08
$NpO_2^+ + CO_3^{2-} \Leftrightarrow NpO_2CO_3^-$	4.96	[1]	−4	−0.65
$NpO_2^+ + 2CO_3^{2-} \Leftrightarrow NpO_2(CO_3)_2^{3-}$	6.53	[1]	0	−0.36
$NpO_2^+ + 3CO_3^{2-} \Leftrightarrow NpO_2(CO_3)_3^{5-}$	5.5	[1]	12	−0.07
$NpO_2^+ + CO_3^{2-} + H_2O \Leftrightarrow NpO_2CO_3OH^{2-} + H^+$	−7	[9][a]	0	−0.14
$NpO_2^+ + CO_3^{2-} + 2H_2O \Leftrightarrow NpO_2CO_3(OH)_2^{3-} + 2H^+$	−20.34	[9][a]	6	0.37
$NpO_2^+ + 2CO_3^{2-} + H_2O \Leftrightarrow NpO_2(CO_3)_2OH^{4-} + H^+$	−5.31	[1]	8	0.15
$NpO_2^{2+} + H_2O \Leftrightarrow NpO_2OH^+ + H^+$	−5.1	[1]	−2	0.02
$2NpO_2^{2+} + 2H_2O \Leftrightarrow (NpO_2)_2(OH)_2^{2+} + 2H^+$	−6.27	[1]	−2	0.63
$3NpO_2^{2+} + 5H_2O \Leftrightarrow (NpO_2)_3(OH)_5^+ + 5H^+$	−17.12	[1]	−6	0.96
$NpO_2^{2+} + 2H_2O \Leftrightarrow NpO_2(OH)_2(aq) + 2H^+$	−12.21	[p.w.][b]	−2	0.09
$NpO_2^{2+} + 3H_2O \Leftrightarrow NpO_2(OH)_3^- + 3H^+$	−19.6	[p.w.][b]	0	0.14
$NpO_2^{2+} + 4H_2O \Leftrightarrow NpO_2(OH)_4^{2-} + 4H^+$	−31.6	[p.w.][b]	4	0.65
$NpO_2^{2+} + CO_3^{2-} \Leftrightarrow NpO_2CO_3(aq)$	9.32	[1]	−8	−0.64
$NpO_2^{2+} + 2CO_3^{2-} \Leftrightarrow NpO_2(CO_3)_2^{2-}$	16.52	[1]	−8	−0.81
$NpO_2^{2+} + 3CO_3^{2-} \Leftrightarrow NpO_2(CO_3)_3^{4-}$	19.37	[1]	0	−0.52
$2NpO_2^{2+} + CO_3^{2-} + 3H_2O \Leftrightarrow (NpO_2)_2CO_3(OH)_3^- + 3H^+$	−2.87	[1]	−8	−0.50

a: Original data at $I = 3$ M $NaClO_4$ recalculated in this work considering the approach in [14];
b: Estimated by correlation with Z_{eff}.

Acknowledgment. D. Fellhauer and V. Petrov are kindly acknowledged for the help in sample preparation and UV-vis/NIR measurements. The contribution of N. Banik, C. Marquardt and E. Soballa to the *in-situ* preparation of Np XANES references and SEM-EDS analysis is highly appreciated. Thanks are due to I. Puigdomenech for kindly providing data on $\varepsilon(TMA^+, X^-)$. We also thank the staff at INE-Beamline (ANKA) for their technical assistance. JT, EW and XG acknowledge the funding of NAGRA. The research leading to these results has received funding from the European Union's European Atomic Energy Community's (Euratom) Seventh Framework Programme FP7/2007-2011 under grant agreement No. 212287 (RECOSY project). The study was partly funded by ACTINET-i3 Integrated Infrastructure Initiative.

References

1. Guillaumont, R., Fanghänel, J., Neck, V., Fuger, J., Palmer, D. A., Grenthe, I., Rand, M. H.: *Chemical Thermodynamics Vol. 5. Update on the Chemical Thermodynamics of Uranium, Neptunium, Plutonium, Americium and Technetium*. (OECD, NEA-TDB) Elsevier, North Holland, Amsterdam (2003).
2. Lemire, R. J., Fuger, J., Nitsche, H., Potter, P. E., Rand, M. H., Rydberg, J., Spahiu, K., Sullivan, J. C., Ullman, W. J., Vitorge, P., Wanner, H.: *Chemical Thermodynamics Vol. 4. Neptunium and Plutonium*. (OECD, NEA-TDB) Elsevier, North Holland, Amsterdam (2001).
3. Wahlgren, U., Moll, H., Grenthe, I., Schimmelpfennig, B., Maron, L., Vallet, V., Gropen, O.: Structure of uranium(VI) in strong alkaline solutions. A combined theoretical and experimental investigation. J. Phys. Chem. A **103**, 8257–8264 (1999).
4. Nguyen-Trung, C., Palmer, D. A., Begun, G. M., Peiffert, C., Mesmer, R. E.: Aqueous uranyl complexes. 1. Raman spectroscopic study of the hydrolysis of uranyl(VI) in solutions of trifluoromethanesulfonic acid and/or tetramethylammonium hydroxide at 25 °C and 0.1 MPa. J. Solut. Chem. **29**, 101–129 (2000).
5. Rao, L. F., Srinivasan, T. G., Garnov, A. Y., Zanonato, P. L., Di Bernardo, P., Bismondo, A.: Hydrolysis of neptunium(V) at variable temperatures (10–85 °C). Geochim. Cosmochim. Acta **68**, 4821–4830 (2004).
6. Crea, F., De Stefano, C., Gianguzza, A., Piazzese, D., Sammartano, S.: Protonation of carbonate in aqueous tetraalkylammonium salts at 25 °C. Talanta **68**, 1102–1112 (2006).
7. Ermakov, V. S., Peretrukhin, V. F., Krot, N. N.: Redox potentials of the couples Np(VI)-Np(V) and Pu(VI)-Pu(V) in LiOH solutions. Sov. Radiochem. **19**, 212–213 (1977).
8. Williams, C. W., Blaudeau, J. P., Sullivan, J. C., Antonio, M. R., Bursten, B., Soderholm, L.: The coordination geometry of Np(VII) in alkaline solution. J. Am. Chem. Soc. **123**, 4346–4347 (2001).
9. Neck, V., Kim, J. I.: Solubility and hydrolysis of tetravalent actinides. Radiochim. Acta **89**, 1–16 (2001).
10. Choppin, G. R.: Utility of oxidation state analogs in the study of plutonium behavior. Radiochim. Acta **85**, 89–95 (1999).
11. Grenthe, I., Fuger, J., Konings, R. J. M., Lemire, R. J., Muller, A. B., Nguyen-Trung, C., Wanner, H.: *Chemical Thermodynamics Vol. 1. Chemical Thermodynamics of Uranium*. (OECD, NEA-TDB) Elsevier, North Holland, Amsterdam (1992).
12. Neck, V., Altmaier, M., Rabung, T., Lützenkirchen, J., Fanghänel, Th.: Thermodynamics of trivalent actinides and neodymium in NaCl, $MgCl_2$, and $CaCl_2$ solutions: Solubility, hydrolysis, and ternary Ca-M(III)-OH complexes. Pure Appl. Chem. **81**, 1555–1568 (2009).
13. Neck, V., Fanghänel, Th., Kim, J. I.: Mixed hydroxo-carbonate complexes of neptunium(V). Radiochim. Acta **77**, 167–175 (1997).
14. Hummel, W.: Ionic strength corrections and estimation of SIT ion interaction coefficients. PSI Report TM-44-09-01, Paul Scherrer Institut, Villigen (Switzerland) (2009).

15. Puigdomenech, I.: INPUT, SED, and PREDOM: Computer programs drawing equilibrium diagrams. TRITA-OOK-3010 Royal Institute of Technology (KTH), Dept. Inorg. Chemistry, Stockholm (Sweden) (1983).
16. Hummel, W., Anderegg, G., Rao, L., Puigdomènech, I., Tochiyama, O.: *Chemical Thermodynamics Vol. 9. Chemical Thermodynamics of Compounds and Complexes of U, Np, Pu, Am, Tc, Se, Ni and Zr with Selected Organic Ligands*. (OECD, NEA-TDB) Elsevier, North Holland, Amsterdam (2005).
17. Felmy, A. R., Rai, D., Mason, M. J.: The solubility of hydrous thorium(IV) oxide in chloride media – development of an aqueous ion-interaction model. Radiochim. Acta **55**, 177–185 (1991).
18. Altmaier, M., Metz, V., Neck, V., Müller, R., Fanghänel, Th.: Solid–liquid equilibria of $Mg(OH)_2$(cr) and $Mg_2(OH)_3Cl\,4H_2O$(cr) in the system Mg-Na-H-OH-O-Cl-H_2O at 25 °C. Geochim. Cosmochim. Acta **67**, 3595–3601 (2003).
19. Altmaier, M., Gaona, X., Fellhauer, D., Buckau, G.: Intercomparison of redox determination methods on designed and near-neutral aqueous systems. KIT-SR 7572, Karlsruhe Institute of Technology, Karlsruhe (2010).
20. Dardenne, K., Brendebach, B., Denecke, M. A., Liu, X., Rothe, J., Vitova, T.: New developments at the INE-Beamline for actinide research at ANKA. in 14th International Conference on X-ray Absorption Fine Structure (XAFS14). Camerino, Italy (2009).
21. Denecke, M. A., Rothe, J., Dardenne, K., Blank, H., Hormes, J.: The INE-beamline for actinide research at ANKA. Phys. Scripta T **115**, 1001–1003 (2005).
22. Ravel, B., Newville, M.: ATHENA, ARTEMIS, HEPHAESTUS: data analysis for X-ray absorption spectroscopy using IFEFFIT. J. Synchrotron Radiat. **12**, 537–541 (2005).
23. Rehr, J. J., Albers, R. C.: Theoretical approaches to X-ray absorption fine structure. Rev. Mod. Phys. **72**, 621–654 (2000).
24. Charushnikova, I. A., Krot, N. N., Starikova, Z. A.: Synthesis, crystal structure, and characteristics of double cesium neptunium(IV) sulfate. Radiochemistry **42**, 42–47 (2000).
25. Forbes, T. Z., Burns, P. C., Skanthakumar, S., Soderholm, L.: Synthesis, structure, and magnetism of Np_2O_5. J. Am. Chem. Soc. **129**, 2760–2761 (2007).
26. Loopstra, B. O., Taylor, J. C., Waugh, A. B.: Neutron powder profile studies of gamma-uranium trioxide phases. J. Solid State Chem. **20**, 9–19 (1977).
27. Antonio, M. R., Soderholm, L., Williams, C. W., Blaudeau, J. P., Bursten, B. E.: Neptunium redox speciation. Radiochim. Acta **89**, 17–25 (2001).
28. Ikeda-Ohno, A., Hennig, C., Rossberg, A., Funke, H., Scheinost, A. C., Bernhard, G., Yaita, T.: Electrochemical and complexation behavior of neptunium in aqueous perchlorate and nitrate solutions. Inorg. Chem. **47**, 8294–8305 (2008).
29. Farges, F., Ponader, C. W., Calas, G., Brown, G. E.: Structural environments of incompatible elements in silicate glass melt systems. 2. U(IV), U(V) and U(VI). Geochim. Cosmochim. Acta **56**, 4205–4220 (1992).
30. Conradson, S. D., Al Mahamid, I., Clark, D. L., Hess, N. J., Hudson, E. A., Neu, M. P., Palmer, P. D., Runde, W. H., Tait, C. D.: Oxidation state determination of plutonium aquo ions using X-ray absorption spectroscopy. Polyhedron **17**, 599–602 (1998).
31. Denecke, M. A.: Actinide speciation using X-ray absorption fine structure spectroscopy. Coord. Chem. Rev. **250**, 730–754 (2006).
32. Denecke, M. A., Dardenne, K., Marquardt, C. M.: Np(IV)/Np(V) valence determinations from Np L_3 edge XANES/EXAFS. Talanta **65**, 1008–1014 (2005).
33. Den Auwer, C., Simoni, E., Conradson, S., Madic, C.: Investigating actinyl oxo cations by X-ray absorption spectroscopy. Eur. J. Inorg. Chem. 3843–3859 (2003).
34. Brendebach, B., Banik, N. L., Marquardt, C. M., Rothe, J., Denecke, M. A., Geckeis, H.: X-ray absorption spectroscopic study of trivalent and tetravalent actinides in solution at varying pH values. Radiochim. Acta **97**, 701–708 (2009).
35. Allen, P. G., Bucher, J. J., Shuh, D. K., Edelstein, N. M., Reich, T.: Investigation of aquo and chloro complexes of UO_2^{2+}, NpO_2^{+}, Np^{4+}, and Pu^{3+} by X-ray absorption fine structure spectroscopy. Inorg. Chem. **36**, 4676–4683 (1997).
36. Spencer, S., Gagliardi, L., Handy, N. C., Ioannou, A. G., Skylaris, C. K., Willetts, A., Simper, A. M.: Hydration of UO_2^{2+} and PuO_2^{2+}. J. Phys. Chem. A **103**, 1831–1837 (1999).
37. Shannon, R. D.: Revised effective ionic-radii and systematic studies of interatomic distances in halides and chalcogenides. Acta Crystallogr. A **32**, 751–767 (1976).
38. Denecke, M. A., Marquardt, C. M., Rothe, J., Dardenne, K., Jensen, M. P.: XAFS study of actinide coordination structure in Np(IV)-fulvates. J. Nucl. Sci. Technol. **3**(Suppl.) (2002).
39. Moll, H., Reich, T., Szabo, Z.: The hydrolysis of dioxouranium(VI) investigated using EXAFS and O-17-NMR. Radiochim. Acta **88**, 411–415 (2000).
40. Clark, D. L., Conradson, S. D., Donohoe, R. J., Keogh, D. W., Morris, D. E., Palmer, P. D., Rogers, R. D., Tait, C. D.: Chemical speciation of the uranyl ion under highly alkaline conditions. Synthesis, structures, and oxo ligand exchange dynamics. Inorg. Chem. **38**, 1456–1466 (1999).